Materials Science & Engineering A 820 (2021) 141536

Contents lists available at ScienceDirect

Materials Science & Engineering A

journal homepage: www.elsevier.com/locate/msea

Plasticity and structure evolution of ferrite and martensite in DP 1180 during tension and cyclic bending under tension to large strains

Krishna Yaddanapudi [a], Marko Knezevic [b,*], Subhash Mahajan [a], Irene J. Beyerlein [c]

[a] Department of Materials Science and Engineering, University of California, Davis, CA, 95616, USA
[b] Department of Mechanical Engineering, University of New Hampshire, Durham, NH, 03824, USA
[c] Department of Mechanical Engineering, Materials Department, University of California, Santa Barbara, CA, 93106, USA

ARTICLE INFO

Keywords:
Dislocations
Deformation twinning
Martensite
Ferrite
Continuous bending under tension

ABSTRACT

This paper describes the main results obtained from a detailed experimental investigation into the dislocation and twinned structures that develop in dual phase (DP) steel sheets. In particular, the morphology and defect-structures present in DP 1180 steel having 55% ferrite and 45% martensite, were examined using transmission electron microscopy (TEM). Microstructure of the as-received DP 1180 consists of a twin-free martensite phase in the form of lath and island morphologies and a ferrite phase exhibiting a relatively low dislocation content (3.41×10^8 cm^{-2}). The steel was deformed in simple tension (ST) to fracture and in continuous-bending-under-tension (CBT) to six cycles. As the CBT test facilitates stretching of the sheet considerably beyond the point of necking, strength increases and substantially exceeds that achieved in ST at fracture. As a consequence of plastic deformation, nano-twins are found in the island-shaped martensite, while the lath-shaped martensite remains twin-free. Additionally, some martensite regions develop a needle-like morphology after CBT. As dislocation density in the ferrite matrix increases with plastic strain, dislocation structures and accumulations of dislocations near the ferrite/martensite interface develop in the ferrite. Unlike in the as-received and ST-deformed DP 1180 samples, high density of dislocations (1.47×10^9 cm^{-2}) and dislocation tangles are observed in ferrite regions of the CBT processed sample. We propose that the primary mechanisms enabling the achievement of high strength, while maintaining residual ductility upon CBT are intense plastic slip in the ferrite and profuse nano-twinning in the martensite regions.

1. Introduction

In order to build lighter, better performing, and more crashworthy vehicle structures, advanced-high-strength-steels (AHSS) are being developed and used in designs. Examples of AHSS are steels known as dual-phase (DP) steels. Understanding and optimizing the microstructure of DP steels to achieve higher formability, strength, and work hardening in conjunction with higher energy absorption in crash loading conditions is subject of ongoing research [1–8].

Properties of DP steels are governed by microstructural features such as the volume fraction and distribution of ferrite and martensite phases, texture per phase, grain size, and chemistry i.e. carbon content in martensite regions. The ferrite and martensite phases have slightly different crystal structures but highly contrasting mechanical characteristics. Simultaneous improvement of strength and formability of DP steels is possible by varying the volume fraction and distribution of phases [9–11]. The deformation of DP steels is highly heterogeneous and driven by the evolution of the local stress-strain fields among these phases. Regions of large ferrite grains deform earlier than small ferrite grains [12]. Severe strain localizations and voids form within such large ferrite grains, ferrite channels between martensitic regions, and also at ferrite/martensite interfaces [2,12,13]. Therefore, DP steels can exhibit limited uniform ductility prior to fracture (~10–15%) in sheet forming [14–19].

In a few investigations, it has been shown that the martensite phase in DP steels could deform plastically along with the ferrite, however, the macroscopic strain at which the martensite begins to deform is dependent on various microstructural parameters such as the volume fraction of the martensite and carbon atom content in the martensite phase [20–24]. Low carbon atom content in martensite can make martensite

* Corresponding author. Department of Mechanical Engineering, University of New Hampshire, 33 Academic Way, Kingsbury Hall, W119, Durham, NH, 03824, USA.
E-mail address: marko.knezevic@unh.edu (M. Knezevic).

https://doi.org/10.1016/j.msea.2021.141536
Received 29 November 2020; Received in revised form 27 May 2021; Accepted 28 May 2021
Available online 3 June 2021
0921-5093/

Table 1
Nominal chemical composition of DP 1180 steels (wt.%).

C	Mn	P	S	Si	Cu	Ni	Cr	Mo
0.168	2.222	0.015	0.0053	1.421	0.021	0.007	0.036	0.013
Sn	Al	Zr	V	Nb	Ti	B	N	
0.007	0.051	0.005	0.012	0.007	0.039	0.0004	0.0086	

relatively soft and thus deform plastically. Das et al. [25] observed high dislocation content in martensite regions of DP 800 steel deformed under high strain rate conditions. Mazinani et al. [22,23] also reported that the martensite phases in DP steels with martensite volume fraction higher than 25%, could deform plastically during tensile straining and induce rapid hardening. Recent nanoindentation and micropillar compression tests revealed that the martensite phase in DP steels is amenable to plastic deformation in the early stages of deformation [26]. In addition to the activation of the in-lath-plane slip system, sliding motion of adjacent martensite blocks along the interface was observed [27]. These observations indicate that the martensite phase in DP steels could deform plastically along with the soft ferrite matrix to accommodate a portion of plastic strain during deformation. However, in contrast to the well understood ferrite phase, the actual nature of slip or twinning that is responsible in accommodating the plastic strains in martensite phases remains to be clarified. At the very least, the frequently observed twin structures in martensite phases of various deformed steels suggest that martensite could accommodate strains by mechanical twinning during its formation from the austenite [28–34]. Besides, a number of material models used to interpret and predict the deformation behaviour of DP steels consider the martensite phase to deform elastically [35,36]. In contrast, other material model formulations provided good prediction of strain path reversals in DP steels only after considering the martensite phase to accommodate some plastically [37,38].

In addition to the optimization of microstructure in DP steels for higher ductility, strength, and energy absorption during crash, it is desirable to reduce forming forces in the sheet metal forming operations for reduced energy consumption [39]. Sheet metal forming processes are being innovated to exploit the intrinsic ductility throughout the sheet, avoiding localized necking and subsequent failure triggered by necking. One such innovation is a continuous-bending-under-tension (CBT) process/test, which achieves plastic strains well beyond those in conventional forming limited by necking [40–42]. The beneficial effect of bending superimposed on tension to enhance the stretchability of sheets was observed in Ref. [43], as well as in forming of sheet involving drawbeads [44]. In the CBT process/test, the sheet specimen is cyclically bent and unbent by rollers while pulled in tension. As the deformation is facilitated by the bending in addition to tension, the process deforms a sheet with a much lower force than would be required by solely tension. In CBT, the bending under tension is restricted to the region of the sheet underneath the rollers resulting in an incremental forming conditions. Such conditions delay localization and necking facilitating relatively uniform straining throughout the sheet as opposed to localized deformation via necking. The key difference between the CBT process and simple tension (ST) is in the uniform ductility depletion throughout the sheet in CBT, whereas necking occurs in ST with most the sheet (i.e., outside of the necked region) having ample remaining ductility [45–47]. The concentrated deformation at fracture upon ST has been estimated as similar to the deformation over the entire gauge length of a CBT tested specimen for AA6022-T4 [40,48,49] and even larger for DP steels [50–53]. The CBT process can be interrupted after a certain number of cycles to evaluate achieved strength and any residual ductility in the sheet by secondary ST tests [40,53].

Taking advantages of the improved stretchability achieved by CBT, in this work, we study the plasticity and structure evolution of ferrite and martensite phases in DP 1180 steel at severe strains. To better elucidate the effect of the extreme straining, we investigate the same aspects of the material after testing in ST to fracture. As a reference, we also study the same aspects for the as-received material. We employ transmission electron microscopy (TEM) to examine the structure, morphology, orientation and the defect structure present in the ferrite and martensite regions of these deformed samples as well as the as-received DP 1180. Electron back scattered diffraction (EBSD) and neutron diffraction (NeD) methods were used to examine the texture, grain structure, and martensite morphologies at a coarser scale. The obtained results were compared and discussed in detail to explain the accommodation structures that are responsible for the achievement of high strength, while maintaining residual ductility of DP 1180 upon CBT.

2. Material and experimental methods

2.1. Material

The as-rolled DP 1180 steel sheets studied in the current work were obtained from the US Steel [54]. The sheets came from their continuous annealing line and were received as bare. The chemical compositions is provided in Table 1. Thermo-mechanical processing history and, in particular, the degree of tempering of DP 1180 sheets pertains to the processing recipe at US Steel. Carbon content of the martensitic phase was not measured. The bulk chemistry along with the measured phase fractions and an approximately zero content of carbon in the ferrite can be used to estimate the average value. However, the content varies spatially from early-formed to late-formed martensite during the quenching process [55,56]. Attempting to simultaneously map element distribution locally through reconstructing 3D maps from 3D atom probe tomography measurements and TEM of deformation structures would be a worthy but a challenging task. The sheets had thickness of 1 mm.

2.2. Microstructural characterization methods

EBSD was employed to characterize the initial grain structure and phase fractions and distribution of DP 1180 using a Tescan Lyra3 GMU FIB field emission scanning electron microscope. The scanning was performed using an Edax EBSD detector attached to the SEM. Samples were prepared using SiC papers with 400, 600, 800, and 1200 grit, then polished using water-based diamond suspension of 6 μm, 3 μm, and 1 μm on a TriDent PSA cloth, and finally polished to mirror finish using 0.05 μm colloidal silica on a CHEM 2 pad. Scan step sizes was 0.05 μm. While we have attempted to index martensite as the body-centered tetragonal (BCT) structure, we were only able to index ferrite. The BCT crystal structure of martensite is close enough to the body-centered cubic (BCC) structure of ferrite, which indexed to a high confidence index for both ferrite and martensite.

Neutron diffraction was employed in order to obtain bulk texture measurements. For these measurements, the neutron time-of-flight diffractometer at the High Pressure/Preferred Orientation (HIPPO) beam line at the pulsed neutron spallation source at LANSCE, Los Alamos National Laboratory was used [57,58].

The orientation and defect structure present in ferrite and martensite regions of DP 1180 steels were investigated using TEM, with a JEOL JEM 2100F-AC TEM operating at 200 kV. The TEM lamella were not prepared via conventional mechanical grinding, polishing and the subsequent thinning using PIPS. Instead, to produce high quality lamella without

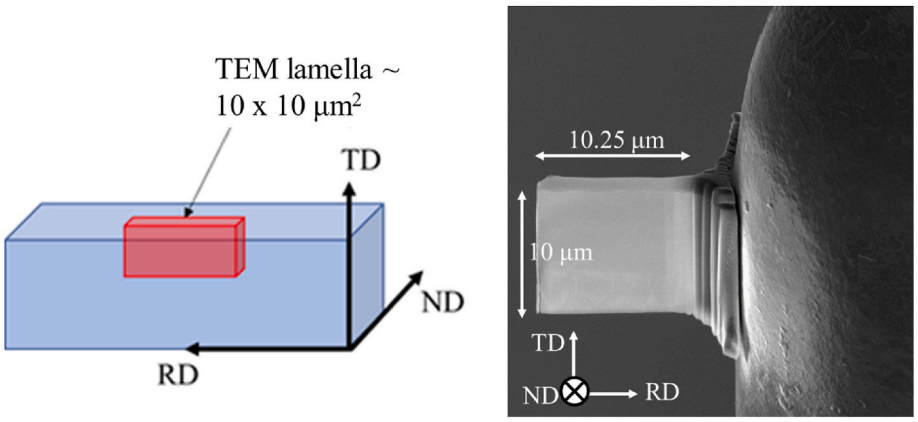

Fig. 1. The prepared TEM lamella in relation to the macroscopic sample directions. All TEM foils investigated in this study have been prepared in the same orientation. The foil plane normal is parallel to the macroscopic sample direction ND. The area of all TEM foils is maintained constantly at ~ 10 × 10 μm².

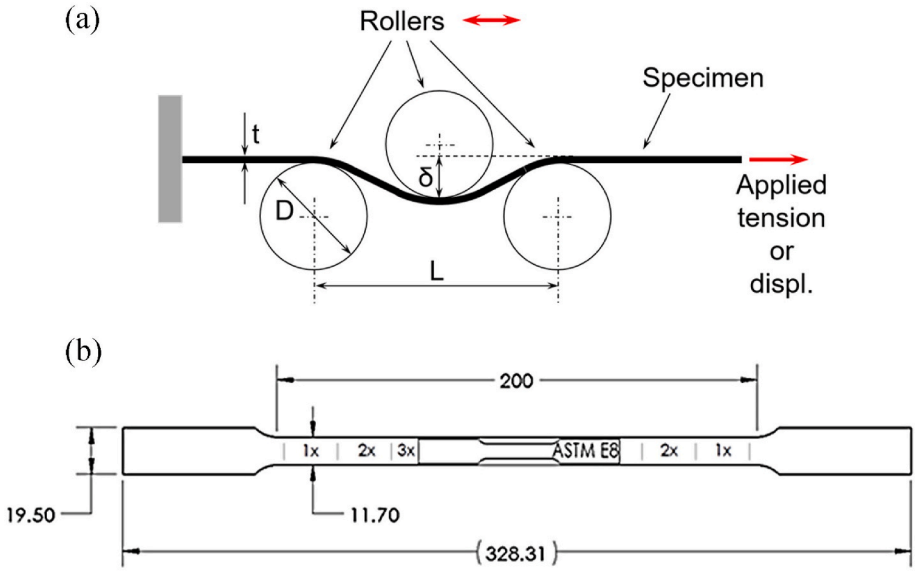

Fig. 2. (a) A schematic of the CBT process with definitions of the main process variables: δ - bending depth, which is set by vertical adjustment of the top roller, t - sheet thickness, D = 25.4 mm - diameters of the rollers, and L = 54 mm - distance between the bottom rollers. (b) Drawing of a specimen used in CBT testing of DP 1180 with the 1 × , 2 × , and 3 × regions and an ASTM E8 sub-size specimen for simple tension (ST) testing to evaluate strength and any residual ductility. Thickness of the specimen is determined by the thickness of the sheet, which is 1 mm. Dimensions are in mm.

mechanical damage, the TEM foils were prepared using FEI Scios dual-beam focused ion beam (FIB), equipped with Ga + ion species as a source. The foil plane normal is parallel to the macroscopic sample direction ND (normal direction) as shown in the schematic of Fig. 1. To clarify further, the TEM observation plane contains TD (transverse direction) and RD (rolling direction). The foil plane area is maintained at ~10 × 10 μm² for all the samples investigated in this study. At least two foils per specimen have been prepared. The ferrite, martensite, and austenite phases in the prepared TEM foils were identified by analysing the selected area electron diffraction (SAED) patterns. The Burgers vectors of the dislocations were determined using the invisibility criteria, where a perfect lattice dislocation becomes invisible or exhibits weak residual contrast when the dot product $\mathbf{g} \cdot \mathbf{b} = 0$, where **g** is the operating reflection used and **b** is the corresponding Burgers vector of the dislocation. The crystallography of twins and their corresponding habit planes were identified by analysing the SAED patterns coupled with the trace analysis.

2.3. Mechanical testing methods

The DP 1180 samples in the as-received state and after six CBT cycles (6 CBT cycles) state were tested in ST using an MTS Landmark 370 servo hydraulic loading-frame equipped with MTS 647 hydraulic grips and relying on the extensometer strain readings. A one-inch MTS 623.12E-24 extensometer was attached to the gauge section of the samples during the tests to gather the displacement data. The tests were carried out at room temperature and at a constant strain rate of 10^{-3} s^{-1}. The tensile samples for the as-received material had standard dimensions with a gauge region of 50.4 mm in length and 11.7 mm in width [59,60]. The geometry and dimensions of the 6 CBT cycles tensile samples are defined in the subsequent paragraphs. The samples were oriented with their loading axis parallel to the rolling direction (RD) of the sheet. Three samples for both ST and 6 CBT were tested with excellent repeatability of results, meaning that the recorded curves were approximately on top of each other.

A brief summary of the CBT process includes a testing device features a moving carriage, which holds a specimen and the axial loading system. The device further has a roller assembly, which is stationary on the machine base. The device is equipped with a data acquisition and control hardware and software. The carriage moves back and force during the CBT test with a velocity of V_{rr} = 66 mm/s, while the sample is loaded in tension. The hydraulic actuator supplies the pulling (i.e. crosshead) velocity. To measure force, load cells are attached to the carriage and to the actuator. These are two donut-style Futek load-cells, one tension (LCF 450, capacity of 22.24 kN) and the other compression (LTH 500, capacity of 22.24 kN). Simultaneously with the carriage motion, the

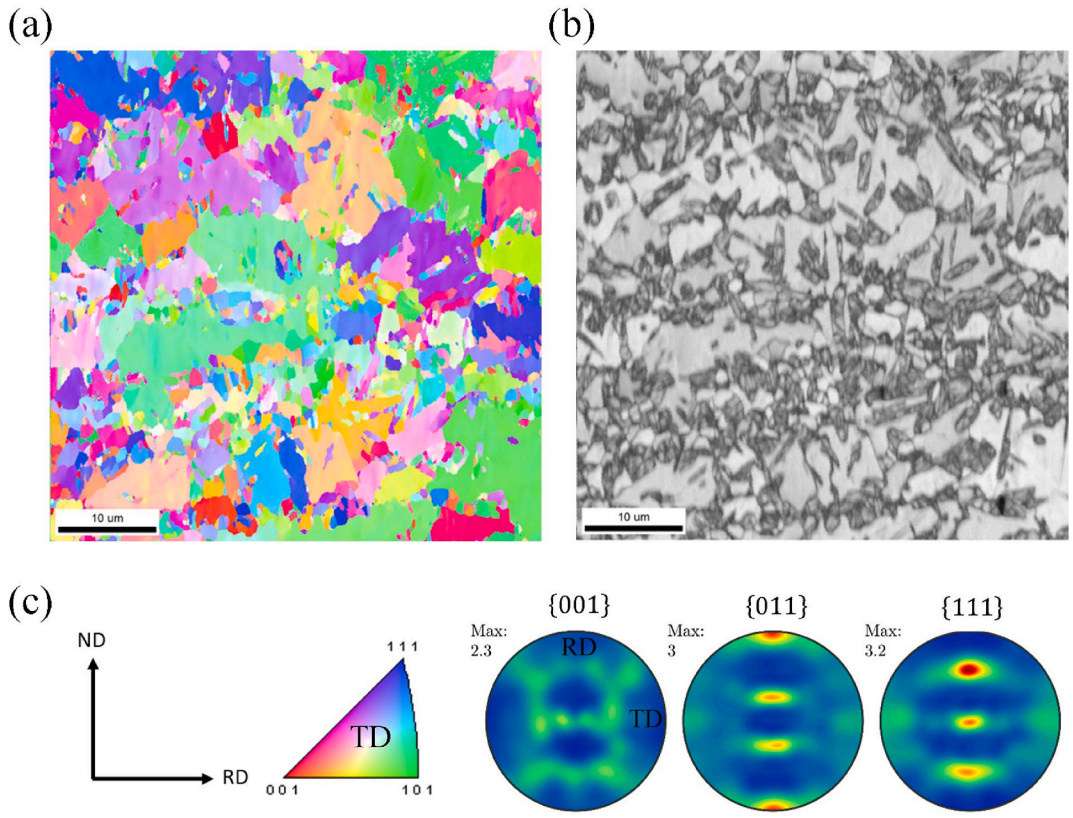

Fig. 3. (a) An inverse pole figure (IPF) map and (b) the corresponding image quality (IQ) map showing the initial microstructure of DP 1180. The coloring in the IPF map represents the orientation of the transverse direction (TD) sample axis, which is perpendicular to the map with respect to the crystal lattice orientation frame according to the IPF triangle. The IQ map reveals martensite phase of ~45% volume fraction. (c) Stereographic pole figures measured by NeD show texture in the initial material.

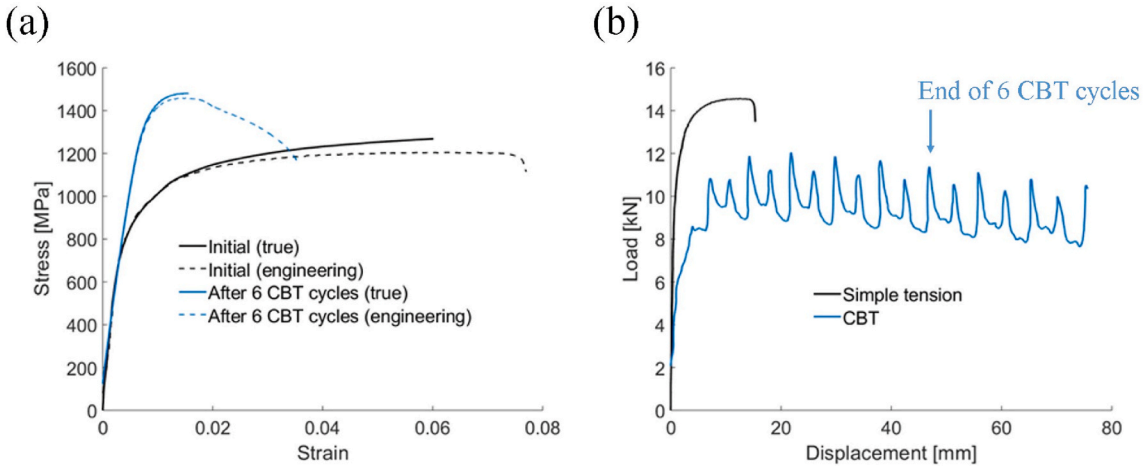

Fig. 4. (a) Stress-strain curves for initial (as-received) and CBT treated to 6 cycles DP 1180 steels along rolling direction (RD) in ST to fracture under a strain rate of 10^{-3} s^{-1} at room temperature. The latter curve shows strength and residual ductility of the material treated by 6 CBT cycles. (b) Load versus displacement curves recorded during ST test and CBT test to fracture along RD. The CBT tests were performed under a set of optimized parameters for maximum elongation of DP 1180: crosshead velocity of 1.35 mm/s, a bending depths of 3.5 mm, and a carriage velocity of 66 mm/s.

roller assembly imposes bending. The top roller is vertically adjustable to impose a bending depth, δ. The carriage motion is limited by limit switches, signalling the end of the stroke and reversion for the carriage motion. We define "a pass or a stroke" to be the rollers traversing the entire gauge length in one direction from one side to the other side of the specimen, while "a CBT cycle" is the rollers traversing the gauge length two times i.e. to the other side and then return back over the gauge section to the initial side. A detailed design of the CBT device was discussed elsewhere [48,61].

Fig. 2(a) and (b) shows the schematic of the CBT process and the selected CBT specimen geometry. The gauge section of 200 mm for the CBT specimen is arbitrarily set. It is chosen such a way that the rollers never exit the gauge section of the standard specimen. Deformation regions indicated as 1x, 2x, and 3x define the number of bending cycles the specimen region undergoes during each CBT pass. In the 1x deformation region is near the grips, the specimen undergoes only one

Table 2
Properties based on the flow curves from Fig. 2(a).

	Initial (as-received)	After 6 CBT cycles
Elastic slope [GPa]	205	206
Yield stress [MPa]	842	1355
UTS [MPa]	1195	1460
Eng. strain at UTS	0.061	0.016
Eng. strain at fracture	0.076	0.035

bending and unbending per pass. In the 2x deformation region, the sheet is bent and unbent two times. Finally, in the 3x deformation region, the sheet is bent and unbent three times. A sub-size specimen machined from the CBT specimen for subsequent ST testing is also shown [59]. The sub-size specimens are ASTM E8 with a gauge section 32 mm in length and 6 mm in width. The sub-size specimens are machined from the 3x region of the interrupted test specimens.

The deformation during CBT involves a through-thickness strain gradient in the bent region of the sheet as the sheet passes over the roller, making direct comparison between ST and CBT strains in the deformation zone underneath the rollers impossible. However, the sheet outside the deformation zone is in pure tension. The central zone of the through-thickness strain gradient experiences monotonic tension till fracture while the other two outermost zones experience ratcheting due to bending-unbending nature of the deformation [62]. Simulations in a

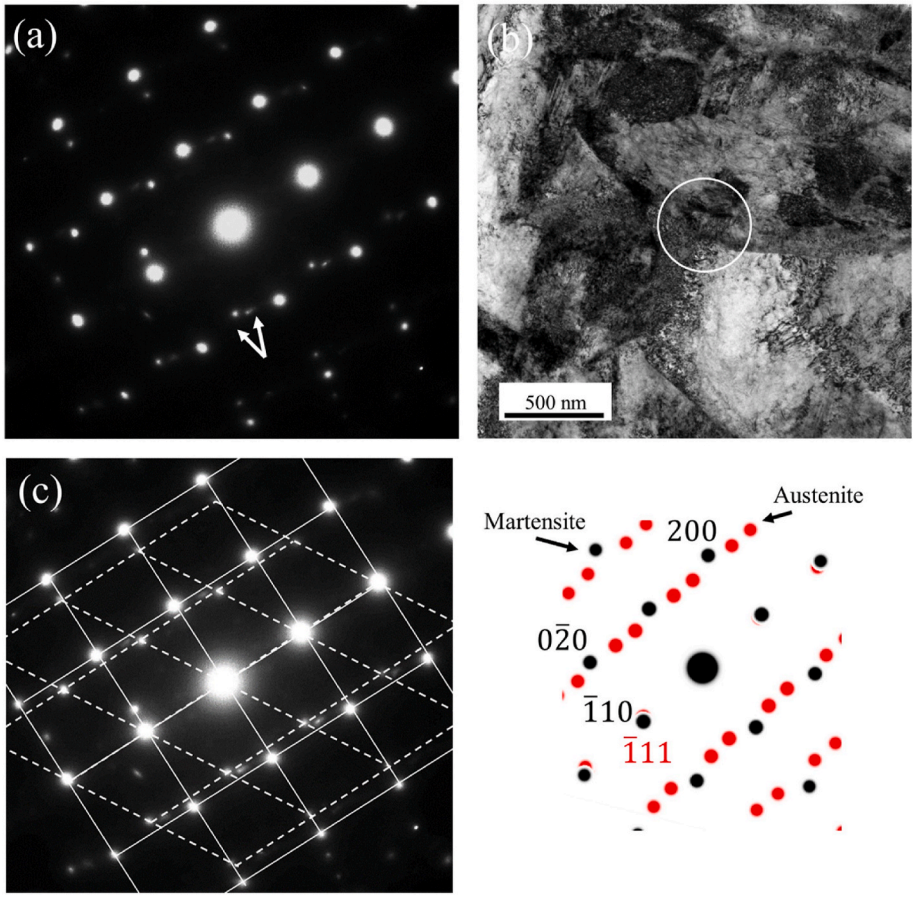

Fig. 5. (a) SAED pattern obtained from a region enclosed by a white circle in the low magnification image shown in (b) for an as-received sample of DP 1180. The white solid lines in (c) indicate the grid corresponding to [001] orientation of martensite, whereas the dashed lines represent the grid corresponding to $[0\bar{1}1]$ orientation of retained austenite for one twin variant. The austenite phase shows the signature of twin variants about $(\bar{1}11)$ plane as indicated by double weak spots (white arrows) in (a). The corresponding simulated diffraction pattern is shown, where the red coloured spots represent austenite, and black coloured spots represent martensite. (For interpretation of the references to colour in this figure legend, the reader is referred to the Web version of this article.)

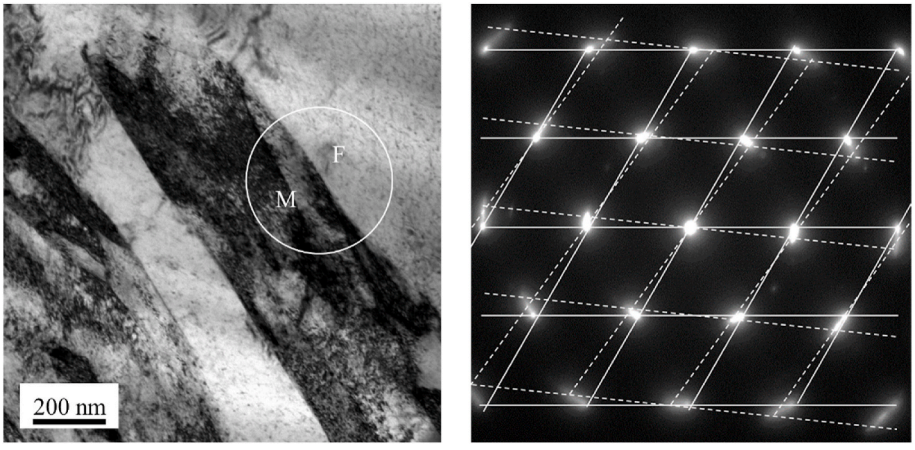

Fig. 6. An SAED pattern acquired from a region enclosed by a white circle consisting of a defective lath-type structure and a defect free ferrite matrix. The SAED pattern is consistent with the [111] orientation of BCC having a lattice constant of 0.286 nm, and a misorientation of 6° about [111] axis. The lath-type structure is identified to martensite and the corresponding diffraction spots are highlighted by white coloured dashed lines, whereas the spots corresponding ferrite are highlighted by white coloured solid lines in the SAED pattern.

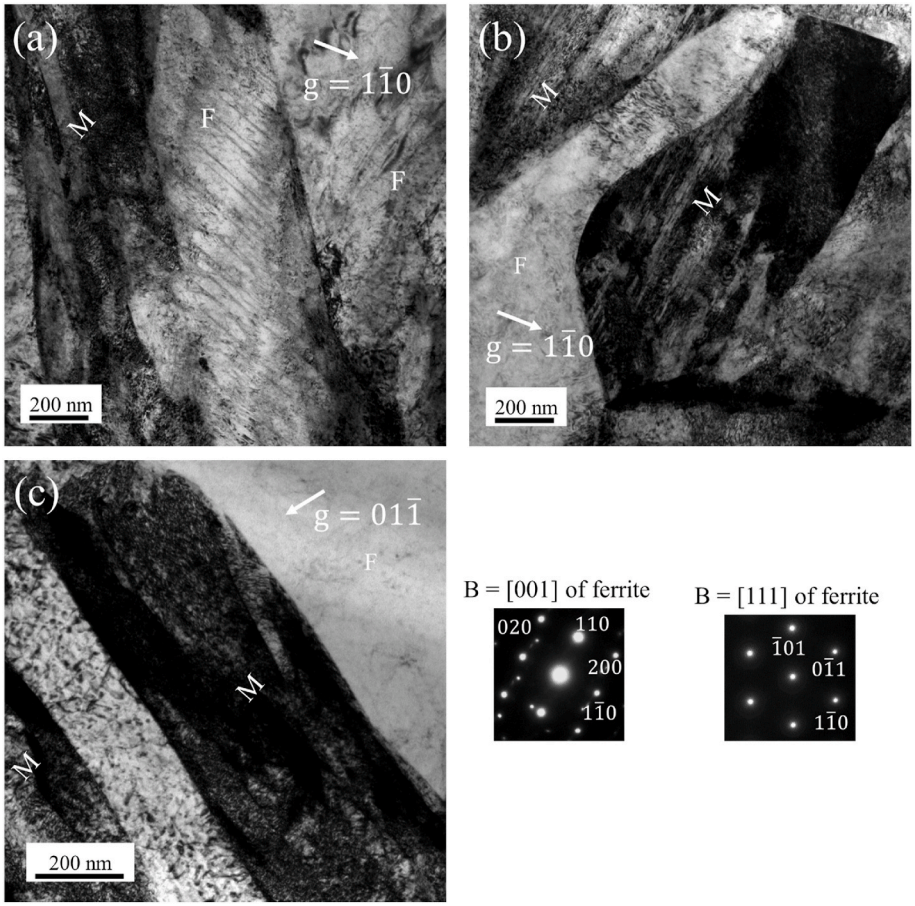

Fig. 7. Two-beam bright field TEM images of the as-received DP 1180 steel microstructure along the B = [001] and [111] orientations of BCC ferrite, and for the operating reflections $\mathbf{g} = 1\bar{1}0$and $01\bar{1}$, where B is the direction of electron beam in TEM. The corresponding SAED patterns are also shown in the Figure. The martensite phase exhibits a lath like morphology in (a), (c), and an island morphology in (b). The martensite regions are found to exhibit strong defect contrast associated with high dislocation content.

Table 3
The observe martensite lath and island size ranges in each of the DP steel samples. The final column displays the dislocation density in ferrite regions of DP steel samples. The average lath size is measured for the martensite laths with sizes higher than 100 nm and lower than 100 nm, and similarly for the martensite islands, the average island size is measured for islands with sizes higher than 500 nm and lower than 500 nm. We have split the lath and island size data into two parts based on our observations. While it is possible to have lath sizes in-between the two mean values in the microstructure, we chose to split the sizes to have more reasonable error bars on the calculated mean values.

Sample name	Average lath size		Average island size		Dislocation density (cm^{-2})
	<100 nm	>100 nm	<500 nm	>500 nm	
As-received	77.7 ± 8	338.3 ± 40	460.5 ± 20	680.2 ± 70	$3.41\pm0.3 \times 10^{8}$
After ST	74.3 ± 6	208.9 ± 35	382.7 ± 37	705.4 ± 42	$1.21\pm0.1 \times 10^{9}$
After CBT	61.8 ± 7	202.8 ± 20	375.3 ± 25	698.4 ± 32	$1.47\pm0.1 \times 10^{9}$

CBT study of 1.4 mm thick DP780 sheet by Barrett et al. [52] revealed that the stress state in the sheet plane is globally uniaxial, since the applied tensile stress is larger than the locally superimposed bending stresses. Importantly, the dominant contributor to effective strain in the sheet is along the tensile direction at every point [52]. The study showed that equivalent plastic strain and axial strain are similar in magnitude during CBT. The effect of through-thickness strain gradients in the present study is also mitigated due to the thinness of the sheet.

A lower bound strain level in the 3x region can be estimated as follows [52]. The gauge length, l, of the CBT specimen is the length that the carriage encompasses (i.e. the length of the roller motion in a pass), $l = \int V_{rr}dt$ (V_{rr} - roller or carriage velocity). The specimen elongates as a consequence of the crosshead motion for $dl \approx \Delta l = \int V_{CH}dt$ (V_{CH} - crosshead velocity). The integrals are calculated numerically from the crosshead and roller velocity experimentally measured profiles. Simply, the strain increment per pass/stroke, $\Delta\varepsilon$, is

$$\Delta\varepsilon = \int \frac{dl}{l} = \frac{\int V_{CH}dt}{\int V_{rr}dt}. \quad (1)$$

In this work, the material was subject to 6 CBT cycles. The CBT tests was performed under a set of optimized parameters for maximum elongation of DP 1180 [51]: crosshead velocity of 1.35 mm/s yielding a quasi-static strain rate varying around 0.001/s, a bending depths of 3.5 mm, and a carriage velocity of 66 mm/s. The strain after 6 CBT cycles is a sum of the strain increments per pass/stroke. The strain per pass is estimated to be $\Delta\varepsilon = 0.0205$, while the strain after 6 CBT cycles (i.e., 12 passes) is $\varepsilon = 0.2455$.

Samples for the TEM investigation are taken from the gauge section near the fractured surface of the broken sample after ST testing and from the 3x region after CBT testing to 6 cycles from approximately middle of the sheet. Note, the CBT sample did not fracture.

3. Results

3.1. Initial microstructure

Fig. 3(a) displays an EBSD image of the microstructure in the form of an inverse pole figure (IPF) map for the transverse direction (TD) sample axis. This observation plane is selected to conveniently reveal any grain elongation in the RD and contraction in the ND. From this map, grains

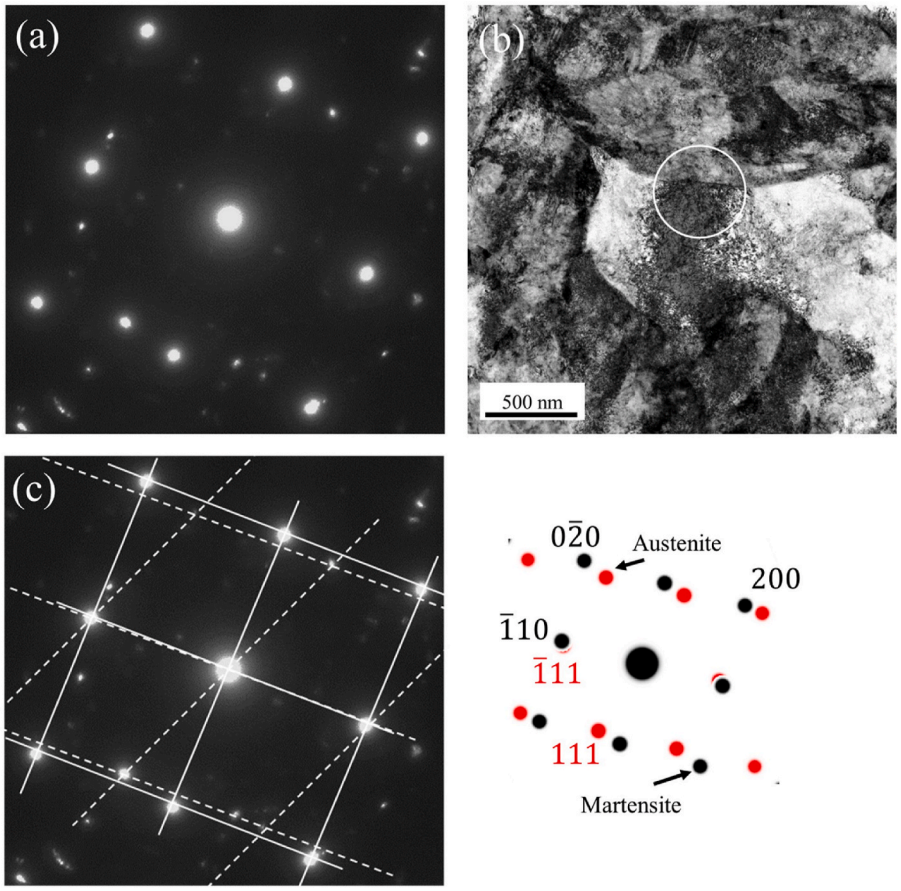

Fig. 8. (a) SAED pattern obtained from a region enclosed by a white circle in the low magnification image shown in (b) for a DP 1180 sample after subjected it to ST deformation. The white solid lines in (c) indicate the grid corresponding to [001] orientation of martensite, whereas the dashed lines represent the grid corresponding to [0$\bar{1}$1] orientation of austenite. The corresponding simulated diffraction pattern is also shown in the figure.

with morphologically rough boundaries and a broad distribution of sizes from ~1 μm to ~20 μm can be observed. To expose the ferrite and martensite phases, we show in Fig. 3(b) an image quality (IQ) map, revealing the distribution of the martensite phases (dark domains) among the ferrite regions (light grey domains). From the map, an approximately 45% volume fraction of martensite phase is estimated. The ratio of 45% martensite and 55% of ferrite is favourable for the study of individual structure evolution. Fig. 3(c) presents the initial texture of DP 1180 using three stereographic pole figures measured by NeD. The starting DP 1180 possesses a conventional rolling texture for body centered cubic (BCC) crystals, with intense γ-fiber and a partial α-fiber [53,63–67].

3.2. Mechanical properties

Fig. 4(a) compares the stress-strain response in ST of the as-received and 6 CBT cycles treated samples of DP 1180 along the RD [51]. It is evident that the CBT treated material is stronger in yield by 61% and ultimate tensile strength (UTS) by 22% when compared to the as-received material (see Table 2). Evidently, the CBT treated material has remaining ductility to continue further CBT testing for additional few cycles (Fig. 4(b)) as well as for the subsequent ST (Fig. 4(a)). The plastic deformation in ST is only from tension, while in CBT is from a combination of bending and tension. Therefore, the tensile load cell records lower magnitudes of load in CBT than in ST. While uniform strain and strain at fracture for the CBT treated material is lower than the as-received material, they are appreciably high. Importantly, the strain imparted by CBT (0.2455) is much greater than the strain imparted by ST (0.061) into the as-received material. Deformation structures are characterized for these two strain levels, in addition to the reference zero strain as-received material.

3.3. Deformed microstructures

To understand the deformation mechanisms in martensite and, in particular, those mechanisms in martensite and ferrite enabling high strength while maintaining reasonable ductility after CBT, we carried out a series of TEM investigations. We have examined the deformation structures of the phases that are present in the three categories of DP 1180 steel samples, i.e. as-received, after subjected to ST, and after subjected to CBT deformation treatment for 6 cycles. The shape and size of martensite regions as well as the defect structure present in the three DP 1180 sample categories have been characterized. The following sections describe the results obtained from each of these samples.

3.3.1. Martensite

3.3.1.1. As-received DP 1180. Fig. 5(a) shows an SAED pattern obtained from the central portion (indicated by a white circle) of the as-received DP 1180 microstructure shown in Fig. 5(b). It is found that the SAED pattern consists of spots corresponding to BCC ferrite/body centered tetragonal (BCT) martensite and retained face centered cubic (FCC) austenite. Any FCC contribution to the observed NeD signal was indistinguishable from background noise, which indicates the lack of presence or, at most, trace quantities of FCC. The strong spots represent the BCC ferrite/BCT martensite along the [001] orientation, as indicated by white solid lines in Fig. 5(c). The magnitude of the associated $\mathbf{g}_{hkl}$ vectors and the angular relationships between them in the SAED pattern is

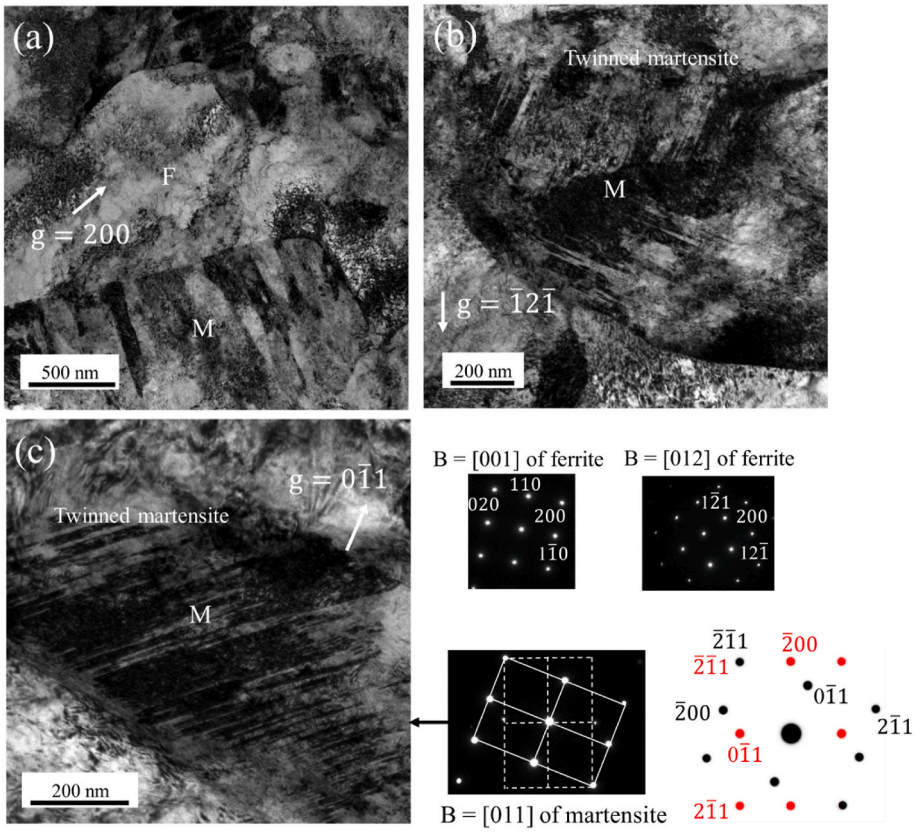

Fig. 9. TEM bright field micrographs of DP 1180 steel microstructure after being subjected to ST. The images were acquired along (a) B = [001] and (b) [012] orientations of ferrite, and for (c) [011] orientation of martensite. The martensite phase exhibits a lath like morphology in (a) as well as twinned morphology in (b) and (c). The diffraction pattern corresponding to twinned martensite is shown in (c) for the [011] orientation of martensite along with the simulated pattern.

consistent with the BCC phase with a lattice constant of 0.286 nm. Importantly, the SAED patterns in this study did not reveal the tetragonal nature of martensite structure, a discrepancy that could be attributed to the relatively low carbon concentration in the studied material (see Table 1). Consequently, the SAED patterns obtained for BCC ferrite and BCT martensite are not significantly different. On the other hand, we find that the weak spots in the SAED pattern are consistent with the $[0\bar{1}1]$ orientation of a retained austenite with a lattice constant of 0.357 nm. The weak intensity of diffraction spots suggests the small fraction of austenite in the material. Moreover, the SAED pattern corresponding to austenite exhibits a signature of twinning as indicated by the double spots (v-shaped white arrow) in Fig. 5(a), and the red-coloured spots in the simulated pattern. The diffraction analysis confirms $(\bar{1}11)$ as the twinning plane of the austenite. The white coloured dashed lines shown in Fig. 5(c) represent one twin variant of FCC austenite. From the diffraction analysis, the following orientation relationship (OR) was obtained between BCC ferrite/martensite and FCC austenite phases: $(\bar{1}10)_M||(\bar{1}11)_A$. This OR is consistent with the commonly observed Kurdjumov-Sachs OR between BCC and FCC phases [6,68–71].

We have identified the martensite and ferrite regions by careful examination of the morphology and orientation. Fig. 6 shows an SAED pattern acquired from a region enclosed by a white circle consisting of a highly defective lath structure exhibiting a morphology of martensite and a defect free ferrite region. The SAED pattern acquired is consistent with the [111] orientation of both regions with a BCC lattice constant of 0.286 nm, however, with a slight misorientation of 6° about [111] axis. The defective lath structure is identified to be a martensite region in the matrix of defect free ferrite region. In the SAED pattern the diffraction spots corresponding to these regions are highlighted by white coloured solid (ferrite) and dashed lines (martensite). Such analysis has been applied to identify the martensite and ferrite regions of the DP steel samples investigated in this work.

Fig. 7 shows the bright field TEM images of the as-received DP1180 microstructure, acquired along the [001] and [111] orientations of BCC ferrite, and for the operating reflections $\mathbf{g} = 1\bar{1}0$, $01\bar{1}$. The martensite phase in the as-received material comes in two shapes, either a lath morphology as highlighted in Fig. 7(a) and (c) or an island morphology, as seen in Fig. 7(b). The average lath thickness and average island size observed in this study for all the DP steel samples are tabulated in Table 3. It is observed that both the lath-shaped and island-shaped martensite exhibit relatively strong defect contrast associated with high dislocation content, which originates from prior processing. In contrast, the BCC ferrite exhibits relatively low dislocation content, as described in section 3.3.2.

Although we have examined the morphology and orientation of martensite regions, the high defect contrast present in these regions makes it difficult to obtain a well-defined Kikuchi pattern and the subsequent alignment to two-beam conditions. As a consequence, it is difficult to establish the exact orientation of electron beam with respect to martensite, which further prevents us from investigating the nature of individual dislocations within martensite regions.

3.3.1.2. DP 1180 after ST. Fig. 8(a) shows an SAED pattern obtained from the DP 1180 microstructure (enclosed by a white circle) shown in Fig. 8(b), which has undergone ST deformation treatment. It is found that the SAED pattern is similar to the diffraction pattern shown in Fig. 5 (a) for the as-received material; however, the spots corresponding to the FCC austenite exhibit weaker intensity and some of the spots are not completely visible. This is attributed to the small fraction of austenite. We have carefully identified the spots belonging to each of the phases and these are represented by white coloured solid and dashed line grids in Fig. 8(c) for the [001] orientation of BCC ferrite/martensite and for

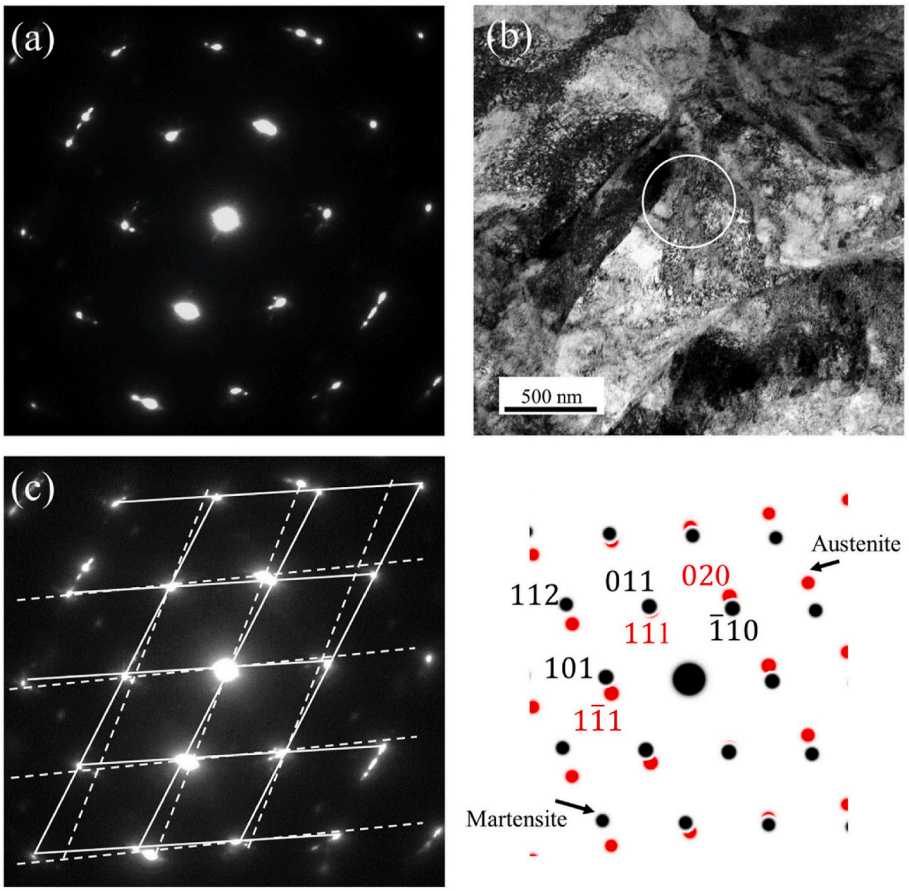

Fig. 10. (a) SAED pattern obtained from a region enclosed by a white circle in the low magnification image shown in (b) for a sample of DP 1180 after CBT testing for 6 cycles. The white solid lines in (c) indicate the grid corresponding to $[\bar{1}\bar{1}1]$orientation of martensite, whereas the dashed lines represent the grid corresponding to $[\bar{1}01]$ of austenite. The corresponding simulated pattern is also shown in the figure for the same orientations.

the $[0\bar{1}1]$ orientation of FCC austenite. The magnitude of the associated $\mathbf{g}_{hkl}$ vectors and the corresponding angular relationships between them is consistent with the BCC phase with a lattice constant of 0.287 nm, and FCC phase with a lattice constant of 0.358 nm. It is further observed that the diffraction pattern is consistent with the OR observed for the BCC phase and FCC austenite in the as-received DP 1180 sample in the preceding section, i.e., $(\bar{1}10)_M||(\bar{1}11)_A$, which is of Kurdjumov-Sachs type.

Fig. 9 shows bright field TEM images of the martensite microstructure acquired from different regions of the same DP 1180 ST deformed sample. The images were acquired along the [001] and [012] orientations of BCC ferrite, and [011] orientation of the martensite. Like the as-received DP 1180 sample, the martensite phase is observed to present in two shapes, island-shaped domains (Fig. 9(b) and (c)) and lath-like domains (Fig. 9(a)). The average lath thickness provided in Table 3, is lower when compared to the as-received DP steel, suggesting that the lath-shaped martensite deformed slightly as a result of the ST deformation. Several other differences, even more significant, are found between the microstructures before and after ST. First, $\{\bar{2}\bar{1}1\}<\bar{1}1\bar{1}>$ type nano-twins are found in the island-shaped martensite phases. These twins contribute to hardening of the phase and the overall material. The SAED pattern obtained from one such twinned martensite region is shown in Fig. 9(c), where the white coloured dashed line grid represents the spots corresponding to twinned martensite. The diffraction analysis indicates that the fine twins observed in the martensite regions of this study exhibit $(\bar{2}\bar{1}1)$ as the habit plane, with a possible twinning system: $\frac{1}{6}[\bar{1}1\bar{1}](\bar{2}\bar{1}1)$. It should be noted that these nano-twins are formed as a result of deformation since they were lacking in the material prior to ST testing. Furthermore, they are not found in the lath-shaped martensite, which possess finer domains than the island-shaped phases. Therefore, it appears that the morphology of the phase governs the selection of active deformation mechanisms.

3.3.1.3. DP 1180 steel after 6 CBT cycles. Fig. 10(a) shows an SAED pattern acquired from the central region of the microstructure shown in Fig. 10(b), of the DP 1180 sample after subjected to CBT deformation for 6 cycles. The diffraction pattern is consistent with the $[\bar{1}\bar{1}1]$ orientation of the BCC ferrite/martensite and the $[\bar{1}01]$ orientation of retained FCC austenite phases as described in the simulated pattern. The phase of austenite did not transform into martensite even after severe straining. The austenite is likely high in carbon content and quite strong and stable in lath form. The experimental SAED pattern has been indexed and is represented by white coloured solid lines and dashed line grids for the BCC ferrite/martensite and FCC austenite phases in Fig. 10(c). The subsequent diffraction analysis reveals that the OR between FCC and BCC phases is $(011)_M||(111)_A$, which is again similar to the ORs observed for the as received and ST deformed DP 1180 samples in the preceding sections.

Fig. 11 shows the morphology of martensite structures acquired from the same DP 1180 sample, which has undergone CBT treatment for 6 cycles. The images were acquired along the $[\bar{1}1\bar{1}]$ and [011] direction of BCC ferrite and for various operating reflection. It is observed that the martensite phase in this case exhibits three kinds of morphology: lath-kind of morphology which is similar to the case of as-received sample and ST-deformed sample (Fig. 11(a) and (b)), twinned morphology which is similar to the case of DP 1180 after ST (Fig. 11(d) and 11(e)), and thin needle-kind of morphology as seen in Fig. 11(c). As noted in

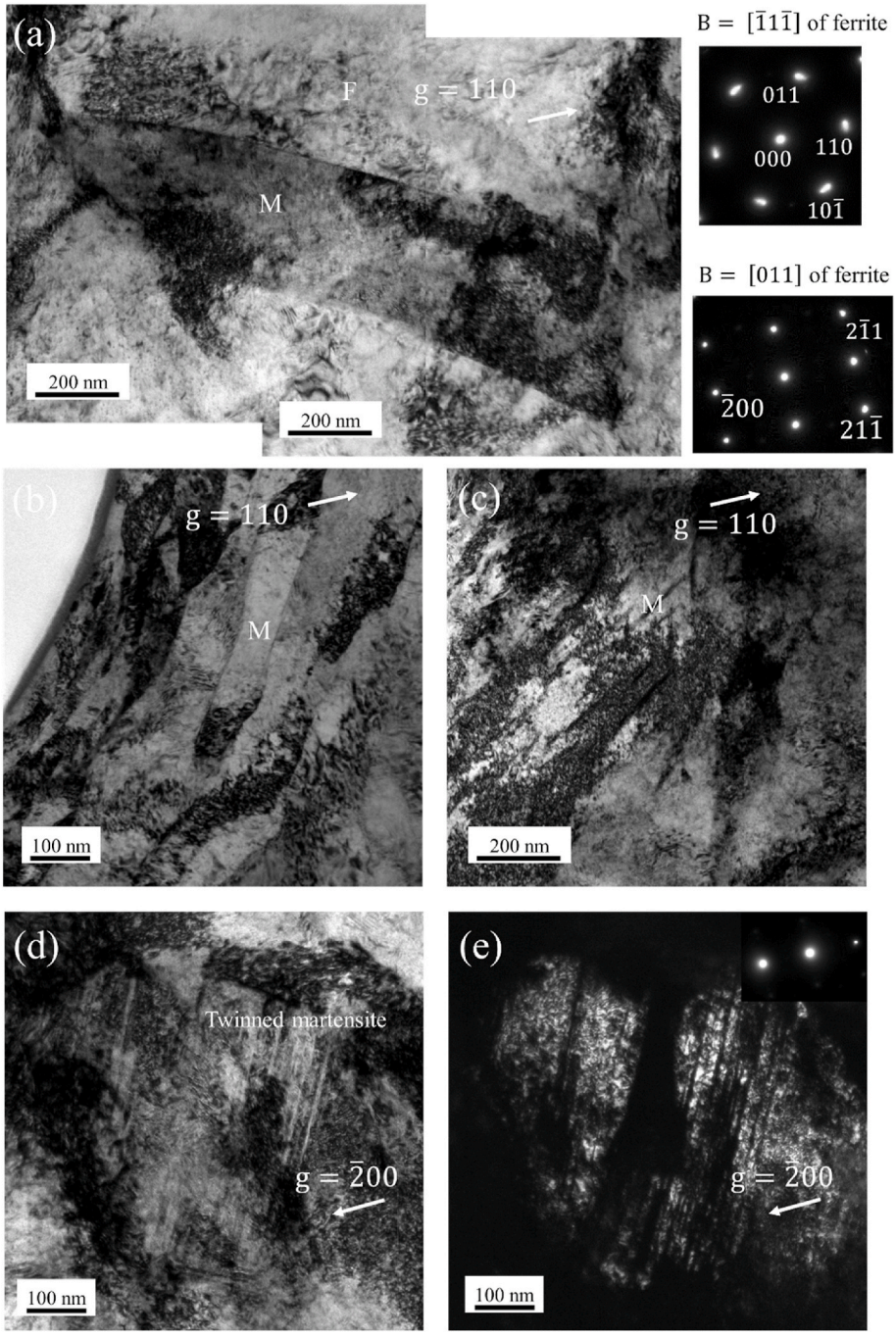

Fig. 11. Bright field TEM micrographs of the DP 1180 steel microstructure after subjected to 6 cycles of CBT. The images were acquired along the (a), (b), (c) B = $[\bar{1}1\bar{1}]$, and (d), (e) B = [011] direction of ferrite, and for the operating reflections $\mathbf{g} = 110$, and $\bar{2}100$. The martensite phase exhibits twinned morphology and lath morphology. The centered dark field image in (b) has been acquired using the $\mathbf{g} = \bar{2}00$ reflection of ferrite.

previous case, nano-twins of $\{\bar{2}11\}\langle\bar{1}1\bar{1}\rangle$ type were observed in the martensite phase and are shown in Fig. 11(d) and (e). Fig. 11(e) shows the centered dark field image of twin structure shown in Fig. 11(d) of martensite region and is acquired using the $\mathbf{g} = \bar{2}00$ reflection of ferrite. These twins may be formed to accommodate the plastic strains developed during CBT deformation contributing to hardening.

3.3.2. *Ferrite and martensite/ferrite interface*

In order to understand the behaviour of DP 1180 deformation, we also examined the defect structure present in the interior of ferrite regions and close to ferrite/martensite interface regions. Fig. 12 shows the structure of $\frac{1}{2}\langle 111\rangle\{\bar{2}11\}$ type and $\frac{1}{2}\langle 111\rangle\{\bar{1}10\}$ type dislocations present in the interior of ferrite regions (i.e., away from the ferrite/martensite interface) of three DP steel samples. The striking difference observed in Fig. 12(a)-12(c) is the increase in dislocation density from the as-received sample to the ST deformed and CBT deformed samples. The dislocation density in these samples was measured using the well-known line-intercept method [72] and the extracted dislocation density in the ferrite regions of all the three DP steel samples is provided in Table 3. The ferrite regions in the as-received sample (Fig. 12(a)) are observed to consist of dislocations having distinct structure and low density when compared to the ST and CBT treated samples (see Table 3).

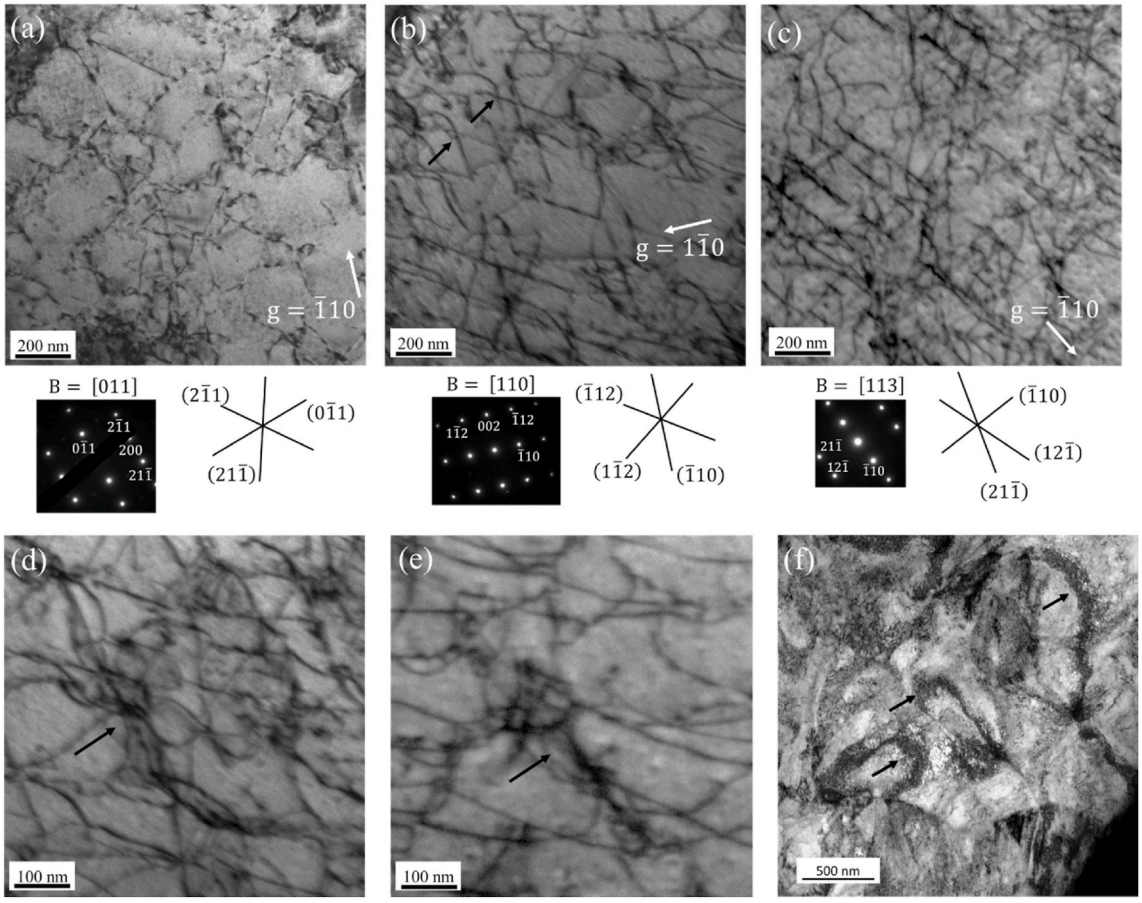

Fig. 12. Two-beam bright field images showing the structure of dislocations formed in the interior of ferrite regions (away from the martensite) of (a) as received DP 1180, (b) DP 1180 sample after ST, and (c) DP 1180 sample after CBT deformation processes. Unlike the as-received, and ST deformed samples, dislocation tangles were observed in the ferrite regions of CBT treated sample and are highlighted by black arrows in (d–f).

In contrast, the ferrite regions of the ST deformed sample (Fig. 12(b)) consist of relatively high dislocation density (1.21×10^9 cm^{-2}). It can be seen that the projected line segments of these dislocations are parallel to the traces of $(\bar{1}12)$ and $(\bar{1}10)$planes (see Fig. 12(b)). The dislocations gliding on these planes are also found intersecting with each other as indicated by the black arrows in Fig. 12(b).

After CBT deformation, the dislocation density is observed to increase further (1.47×10^9cm^{-2}) and most of these dislocations found intersecting each other as noticed in Fig. 12(c). The trace analysis confirms that these dislocations glide on multiple planes such as $(21\bar{1})$,$(12\bar{1})$ and $(\bar{1}10)$ planes and interacting with each other. These results suggest that CBT deformation results in a slight increase in dislocation content in the interior of ferrite regions with a complex structure. The slight increase in dislocation density is possibly due to the severe deformation incurred in the CBT process. Further careful examination of dislocation structures reveals the formation of dislocation tangles in the ferrite regions of CBT deformed sample as shown in Fig. 12(d) and (e)). These tangles are found to exhibit loop-kind of structure as indicated by the black coloured arrows in the low magnification picture (Fig. 12(f)). Such dislocation tangles were not observed in the as-received and ST deformed sample. In earlier studies, it was shown that dislocation tangles can form in ferrite under high plastic strains and result in the form of cell structures [73]. Therefore, it is likely that the strength increases after 6 cycles of CBT is due to the formation of high density of dislocation structures and their tangles.

We have also examined the dislocation structures in ferrite regions away from the tangles of the same DP 1180 CBT sample (Fig. 13), where the ferrite is oriented along the [011] direction as noted from the SAED patterns. The dislocations were imaged under two-beam bright field conditions for various operating reflections as noted on the micrographs. It can be seen that the dislocations that are visible (indicated by black arrows) for the operating reflections $\mathbf{g} = 200$, and $\mathbf{g} = 21\bar{1}$ (for [011] orientation) in Fig. 13(a) and (b), are invisible for the reflection $\mathbf{g} = 2\bar{1}1$ in Fig. 13(c). These observations are consistent with assigning the following Burgers vector $\frac{1}{2}$ [11$\bar{1}$] to these dislocations. Moreover, the projected line segments of these dislocations are found be to parallel to the trace of $(2\bar{1}1)$ plane as indicated by the white coloured dashed lines in Fig. 13(a) and (b). The TEM analysis, thus, confirms the following slip system for dislocations present in ferrite regions: $\frac{1}{2}$ [11$\bar{1}$]$(2\bar{1}1)$. Moreover, the projected line dislocations are parallel to [11$\bar{1}$] direction, as indicated by the red coloured arrow on the micrograph. The red arrow represents the projection of [11$\bar{1}$] direction on the plane of the micrograph. The TEM analysis, therefore, confirm that the dislocations in ferrite regions are in screw orientation, suggesting that these dislocations could move and have participated in the deformation process.

Finally, we have examined the defect structures present in ferrite regions close to ferrite/martensite interface. Fig. 14 shows the dislocation structures in ferrite regions and they found interacting with the ferrite/martensite interface. These dislocations are indicated by black arrows in Fig. 14(a) and (b) for the as received and ST deformed samples. In contrast, strong defect contrast is observed at the ferrite/martensite interface of the CBT deformed sample in Fig. 14(c). The corresponding magnified image (indicated by an orange-coloured box) shows high density of dislocations interacting with ferrite/martensite interface, indicating that these dislocations may be the result of severe plastic deformation in CBT process. Moreover, they were absent in the as

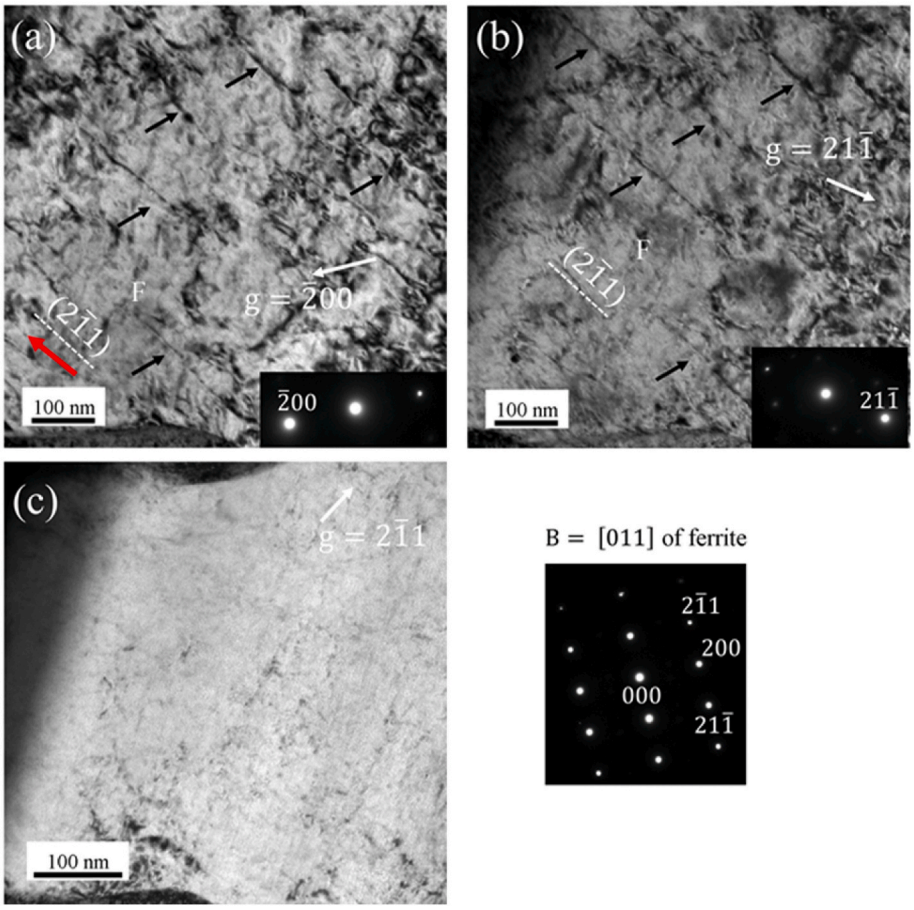

Fig. 13. Dislocation structures formed in the ferrite regions away from the tangle structures shown in Fig. 12 of the same DP 1180 steel after 6 CBT cycles. The images were acquired along the [011] direction of BCC ferrite, and for various operating reflections as indicated on the micrographs. The diffraction contrast analysis reveals that the dislocations indicated by black arrows are screw dislocations lying on the (2$\bar{1}$1) plane and exhibit $\frac{1}{2}$ [11$\bar{1}$] Burgers vector.

received and ST deformed sample.

4. Discussion

The findings described in the current study show that the DP 1180 steel achieves a very high strength under CBT while maintaining residual ductility. The deformation mechanisms responsible for achieving such improved strength under CBT are rationalized in this work and are compared with the ST deformed and as received DP steels. The TEM investigations show that the deformation modes that are observed in DP 1180 steel after CBT are the intense dislocation slip (1.47×10^9 cm^{-2}) in ferrite regions and the mechanical twinning in island-shaped martensite regions, while the lath-shaped martensite regions appear to deform by changing their lath sizes with no mechanical twinning. We found that, in contrast to the CBT process, the ST deformed sample exhibits the same deformation modes, however, with a slight decrease in dislocation content in ferrite regions (1.21×10^9 cm^{-2}, see Table 3), and in ferrite regions adjacent to martensite (see Fig. 14). The as received DP 1180 exhibits low dislocation density in ferrite regions (3.41×10^8 cm^{-2}) with no mechanical twinning in martensite. These observations indicate that CBT process deforms the DP 1180 severely, and the plastic strains generated during CBT appears to be accommodated by the intense dislocation slip in ferrite regions as well as mechanical twinning and slip in martensite regions.

The microstructure of the deformed ferrite regions (i.e., away from the martensite) after CBT process consists of high density of $\frac{1}{2}[1\bar{1}1](21\bar{1})$, $\frac{1}{2}[\bar{1}11](12\bar{1})$ and $\frac{1}{2}[111](\bar{1}10)$ type dislocations interacting with each other and resulting in the formation of dislocation tangles (see Fig. 12 (c)-12(f)). It was reported that dislocation tangles in ferrite grains of DP steels could be formed, when they are allowed to deform at high strains under ST [73]. However, in the current study dislocation tangles were not observed in the as received and ST deformed DP 1180 samples. In contrast to ferrite, the deformation mechanisms in martensite are shape dependent. The island-shaped martensite regions are found to consist of $\frac{1}{6}[\bar{1}1\bar{1}](2\bar{1}1)$type nano-twins associated with high dislocation content, whereas the lath-shaped martensite remains twin free.

Korzekwa et al. reported that slip in ferrite regions of DP steels deformed under ST is inhomogeneous, with higher dislocation density in ferrite regions adjacent to martensite than in ferrite regions away from the martensite [73]. This inhomogeneity in dislocation density is attributed to plastic incompatibility between martensite and adjacent ferrite regions. The current study observes higher dislocation content in the ferrite regions adjacent to martensite when deformed under CBT (Fig. 14(c)), than the ferrite regions deformed under ST and the as received sample (Fig. 14(a) and (b)).

In contrast to BCC ferrite, the plastic behaviour of BCT martensite has been suggested to be dependent on the factors like the carbon content and the volume fraction of martensite in DP steels [20–24]. High volume fraction coupled with low carbon content is suggested to be a favourable situation for the plastic behaviour of martensite. The results in the current study report that for the given nominal carbon content, the island shaped martensite could deform under ST and CBT process by $\frac{1}{6}[\bar{1}1\bar{1}](2\bar{1}1)$ type mechanical twinning. The mechanical twins are observed to associate with high dislocation content. In contrast, no twins were observed in the lath-shaped martensite regions deformed under ST and CBT processes. Instead, the lath-shaped martensite appears to

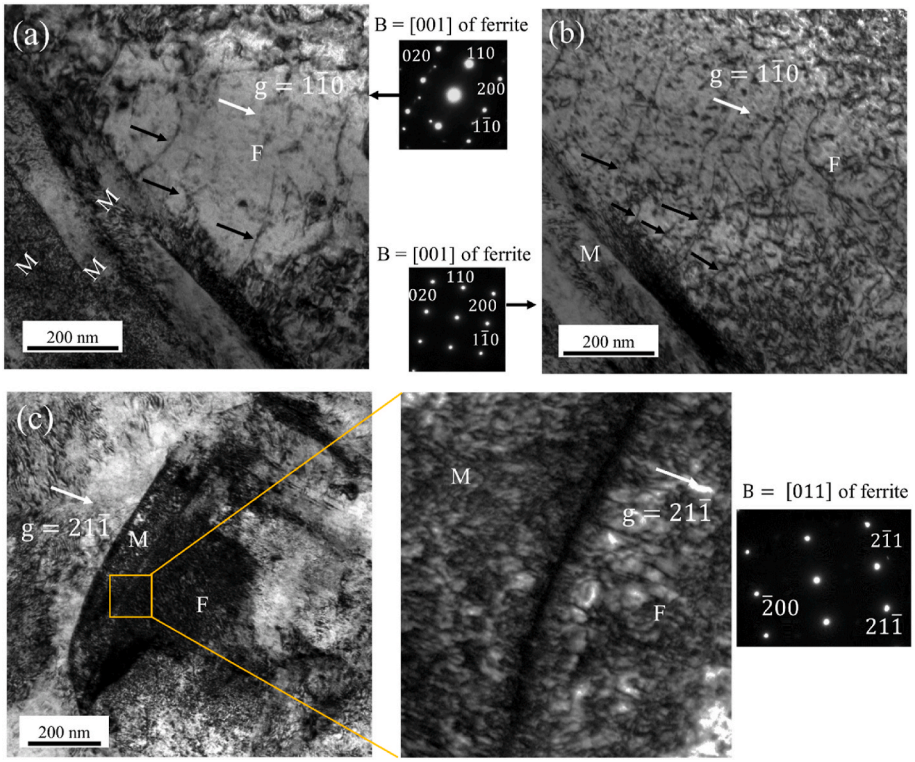

Fig. 14. TEM bright field images showing the structure of dislocations in ferrite regions adjacent to martensite. The dislocations are indicated by black arrows for (a) as received DP 1180 sample, and (b) the sample after ST deformation. In contrast to these, the ferrite adjacent to martensite after CBT exhibits strong defect contrast associated with high dislocation content in (c). The magnified image in (c) shows the high density of dislocations at the ferrite/martensite interface of DP 1180 after CBT.

deform by changing its lath size (likely by slip) under ST and CBT processes. The observed change in average lath size is displayed in Table 3 in comparison to the lath size in the as-received DP 1180 sample. These observations indicate that for the given nominal carbon content (see Table 1), the martensite could deform by twinning and some slip to accommodate at least a portion of plastic strain developed during ST and CBT processes.

The origin of twinning in BCT martensite can be rationalized from the twinning mechanism in BCC crystals. Basically two different approaches were developed for the nucleation of deformation twins [74]. The first one considers the nucleation at a defect site, whereas the second one considers the nucleation by homogeneous lattice shear in a region of high stress concentration [74]. It was shown that twin fault layers in BCC crystals could form by the dissociation of a single lattice $\frac{1}{2} < 11\bar{1} >$ screw dislocation into 3 x $\frac{1}{6} < 11\bar{1} >$ twinning dislocations on the three equivalent $\{2\bar{1}1\}$ planes that intersect symmetrically about the direction of the Burgers vector [75]. The glide of these twinning dislocations, under suitable stress, in the direction of twinning shear develops a twin [75]. A similar mechanism may be expected for the formation of $\frac{1}{6}[\bar{1}1\bar{1}](\bar{2}\bar{1}1)$ twins in BCT martensite. Although we did not study the nature of individual dislocations, the strong defect contrast confirms high dislocation densities in the martensite regions, which could act as a precursor to $\frac{1}{6}[\bar{1}1\bar{1}](\bar{2}\bar{1}1)$ twinning in martensite. Interestingly, in contrast, some martensite regions evidently accommodated deformation by plastically deforming into a lath shape and not twinning. We can speculate that these regions were not crystallographically oriented well for twinning. Taken together, the primary deformation mechanisms responsible for the achievement of high strength and residual ductility of the CBT treated DP 1180 sample are the intense slip occurred in the ferrite regions, and the profuse nano-twinning in the island-shaped martensite regions.

5. Conclusions

This work reveals the plastic deformation mechanisms responsible for the mechanical response of DP 1180 steel deformed by ST and CBT by employing the TEM. Although prior works suggested that the martensite could deform plastically, this work clarifies the actual mechanisms of strain accommodation by martensite regions to very large plastic strains. The reference as-received material is found to consists of twin-free martensite phases of two morphologies, lath and island. In contrast to low density of dislocations in ferrite and ferrite/martensite interface, the martensite phase was found to contain a higher density of dislocations. The analysis of the ST-deformed material reveals that the nanoscale martensite became finer in thickness and deforms by slip and $\frac{1}{6}[\bar{1}1\bar{1}](\bar{2}\bar{1}1)$ nano-twinning. Presence of higher dislocation density at the ferrite/martensite interface after ST than before deformation indicates that the interface served as a barrier to dislocations in the ferrite. Nevertheless, density of dislocations in ferrite substantially increases to initiate the formation of dislocation structures. As the CBT processed material is found substantially stronger with the yield and ultimate tensile strength increase by 61% and 22% relative to ST-deformed material, while also maintaining residual ductility, the controlling mechanisms to enable such behaviour are: $\frac{1}{6}[\bar{1}1\bar{1}](\bar{2}\bar{1}1)$ nano-twinning in the martensite phase and intense and throughout deforming volume spread (i.e. not localised) dislocation slip in ferrite phase. Twins are not observed in the lath-shaped phases, which are finer domains than the island-shaped phases, indicating that morphology of the phase governs the selection of active deformation mechanisms. Moreover, some martensite regions substantially deformed to develop a needle-like morphology contributing to strain accommodation and strength increase. Unlike in the as-received and ST-deformed DP 1180 samples, however, dislocation tangles were observed in the ferrite of the CBT sample. This is evidence of ferrite deforming much more severely in CBT than in ST. The results suggest that the outstanding uniform high strain deformation and strength of CBT processed material stems from well-distributed intense plastic slip in ferrite regions and profuse nano-twinning in the martensite regions. In addition to slip, twins developing in martensite contribute to hardening of the phase and the overall material by barrier effect. Finally, a combination of intense plasticity at interfaces, and tangled dislocation structures in ferrite significantly

harden the softer ferrite phase and effectively harden the overall material.

Data availability

The raw/processed data required to reproduce these findings cannot be shared at this time due to technical or time limitations.

CRediT authorship contribution statement

Krishna Yaddanapudi: Methodology, Formal analysis, Investigation, Visualization, Writing – original draft. **Marko Knezevic:** Conceptualization, Resources, Writing – review & editing, Supervision, Funding acquisition, Project administration. **Subhash Mahajan:** Methodology, Supervision, Funding acquisition. **Irene J. Beyerlein:** Resources, Writing – review & editing, Supervision, Funding acquisition.

Declaration of competing interest

The authors declare that they have no known competing financial interests or personal relationships that could have appeared to influence the work reported in this paper.

Acknowledgements

M. K. acknowledges financial from the U.S. National Science Foundation (NSF) CAREER program (CMMI-1650641). K. Y, S. M., and I. J. B. acknowledge financial support from the NSF Designing Materials to Revolutionize and Engineer our Future (DMREF) program (CMMI-1723539 at UCD and CMMI-1729887 at UCSB).

References

[1] M. Calcagnotto, D. Ponge, D. Raabe, Microstructure control during fabrication of ultrafine grained dual-phase steel: characterization and effect of intercritical annealing parameters, ISIJ Int. 52 (2012) 874–883.
[2] W. Woo, V.T. Em, E.Y. Kim, S.H. Han, Y.S. Han, S.H. Choi, Stress–strain relationship between ferrite and martensite in a dual-phase steel studied by in situ neutron diffraction and crystal plasticity theories, Acta Mater. 60 (2012) 6972–6981.
[3] H. Gong, S. Wang, P. Knysh, Y.P. Korkolis, Experimental investigation of the mechanical response of laser-welded dissimilar blanks from advanced- and ultra-high-strength steels, Mater. Des. 90 (2016) 1115–1123.
[4] B. Ma, Z.G. Liu, Z. Jiang, X. Wu, K. Diao, M. Wan, Prediction of forming limit in DP590 steel sheet forming: an extended fracture criterion, Mater. Des. 96 (2016) 401–408.
[5] A. Ghaei, D.E. Green, A. Aryanpour, Springback simulation of advanced high strength steels considering nonlinear elastic unloading–reloading behavior, Mater. Des. 88 (2015) 461–470.
[6] S. Morito, X. Huang, T. Furuhara, T. Maki, N. Hansen, The morphology and crystallography of lath martensite in alloy steels, Acta Mater. 54 (2006) 5323–5331.
[7] A.M. Cantara, M. Zecevic, A. Eghtesad, C.M. Poulin, M. Knezevic, Predicting elastic anisotropy of dual-phase steels based on crystal mechanics and microstructure, Int. J. Mech. Sci. 151 (2019) 639–649.
[8] A.J. Clarke, J.G. Speer, M.K. Miller, R.E. Hackenberg, D.V. Edmonds, D.K. Matlock, F.C. Rizzo, K.D. Clarke, E. De Moor, Carbon partitioning to austenite from martensite or bainite during the quench and partition (Q&P) process: a critical assessment, Acta Mater. 56 (2008) 16–22.
[9] M. Calcagnotto, Y. Adachi, D. Ponge, D. Raabe, Deformation and fracture mechanisms in fine- and ultrafine-grained ferrite/martensite dual-phase steels and the effect of aging, Acta Mater. 59 (2011) 658–670.
[10] M. Bhargava, S. Chakrabarty, V.K. Barnwal, A. Tewari, S.K. Mishra, Effect of microstructure evolution during plastic deformation on the formability of transformation induced plasticity and quenched & partitioned AHSS, Mater. Des. 152 (2018) 65–77.
[11] A.D. Kudzal, B.A. McWilliams, J. Taggart-Scarff, M. Knezevic, Fabrication of a low alloy ultra-high strength (>1500 MPa yield) steel using powder bed fusion additive manufacturing, Mater. Sci. Eng., A 770 (2020) 138512.
[12] C.C. Tasan, J.P.M. Hoefnagels, M. Diehl, D. Yan, F. Roters, D. Raabe, Strain localization and damage in dual phase steels investigated by coupled in-situ deformation experiments and crystal plasticity simulations, Int. J. Plast. 63 (2014) 198–210.
[13] M. Kapp, T. Hebesberger, O. Kolednik, A micro-level strain analysis of a high-strength dual-phase steel, Int. J. Mater. Res. 102 (2011) 687–691.
[14] R.H. Wagoner, J.H. Kim, J.H. Sung, Formability of advanced high strength steels, Int. J. Material Form. 2 (2009) 359.
[15] H.K.D.H. Bhadeshia, TRIP-assisted steels? ISIJ Int. 42 (2002) 1059–1060.
[16] M. Shi, S. Gelisse, Issues on the AHSS forming limit determination, in: Proceedings of the IDDRG International Conference, Porto, 2006, pp. 19–21. Portugal.
[17] C. Nikhare, P. Hodgson, M. Weiss, Necking and fracture of advanced high strength steels, Mater. Sci. Eng., A 528 (2011) 3010–3013.
[18] N. Saeidi, F. Ashrafizadeh, B. Niroumand, F. Barlat, EBSD study of micromechanisms involved in high deformation ability of DP steels, Mater. Des. 87 (2015) 130–137.
[19] X. Xue, J. Liao, G. Vincze, J. Sousa, F. Barlat, J. Gracio, Modelling and sensitivity analysis of twist springback in deep drawing of dual-phase steel, Mater. Des. 90 (2016) 204–217.
[20] H.P. Shen, T.C. Lei, J.Z. Liu, Microscopic deformation behaviour of martensitic–ferritic dual-phase steels, Mater. Sci. Technol. 2 (1986) 28–33.
[21] T.S. Byun, I.S. Kim, Tensile properties and inhomogeneous deformation of ferrite-martensite dual-phase steels, J. Mater. Sci. 28 (1993) 2923–2932.
[22] M. Mazinani, W. Poole, Effect of martensite plasticity on the deformation behavior of a low-carbon dual-phase steel, Metall. Mater. Trans. 38 (2007) 328–339.
[23] M. Mazinani, W.J. Poole, Deformation behaviour of martensite in a low-carbon dual-phase steel, in: Advanced Materials Research, vol. 15, Trans Tech Publ, 2007, pp. 774–779.
[24] Y.-L. Su, J. Gurland, Strain partition, uniform elongation and fracture strain in dual-phase steels, Mater. Sci. Eng. 95 (1987) 151–165.
[25] A. Das, M. Ghosh, S. Tarafder, S. Sivaprasad, D. Chakrabarti, Micromechanisms of deformation in dual phase steels at high strain rates, Mater. Sci. Eng., A 680 (2017) 249–258.
[26] H. Ghassemi-Armaki, R. Maaß, S. Bhat, S. Sriram, J. Greer, K. Kumar, Deformation response of ferrite and martensite in a dual-phase steel, Acta Mater. 62 (2014) 197–211.
[27] L. Morsdorf, O. Jeannin, D. Barbier, M. Mitsuhara, D. Raabe, C.C. Tasan, Multiple mechanisms of lath martensite plasticity, Acta Mater. 121 (2016) 202–214.
[28] A.G. Crocker, Twinned martensite, Acta Metall. 10 (1962) 113–122.
[29] P. Kelly, J. Nutting, The martensite transformation in carbon steels, Proc. Roy. Soc. Lond. Math. Phys. Sci. 259 (1961) 45–58.
[30] T. Liu, T. Li, X. Liu, TEM and electron diffraction analysis of ω-Fe to cementite transformation in quenched and tempered high carbon steels, AIP Adv. 9 (2019), 045219.
[31] I.B. Timokhina, P.D. Hodgson, E. Pereloma, Transmission electron microscopy characterization of the bake-hardening behavior of transformation-induced plasticity and dual-phase steels, Metall. Mater. Trans. 38 (2007) 2442–2454.
[32] K.-I. Sugimoto, M. Kobayashi, S.-I. Hashimoto, Ductility and strain-induced transformation in a high-strength transformation-induced plasticity-aided dual-phase steel, MTA 23 (1992) 3085–3091.
[33] J. Liu, C. Chen, Q. Feng, X. Fang, H. Wang, F. Liu, J. Lu, D. Raabe, Dislocation activities at the martensite phase transformation interface in metastable austenitic stainless steel: an in-situ TEM study, Mater. Sci. Eng., A 703 (2017) 236–243.
[34] S. Thompson, A transmission electron microscopy investigation of reaustenitized-and-cooled HSLA-100 steel, Metallogr. Microstruct. Anal. 1 (2012) 131–141.
[35] F. Rieger, T. Böhlke, Microstructure based prediction and homogenization of the strain hardening behavior of dual-phase steel, Arch. Appl. Mech. 85 (2015) 1439–1458.
[36] K. Yoshida, R. Brenner, B. Bacroix, S. Bouvier, Micromechanical modeling of the work-hardening behavior of single- and dual-phase steels under two-stage loading paths, Mater. Sci. Eng., A 528 (2011) 1037–1046.
[37] M. Zecevic, Y.P. Korkolis, T. Kuwabara, M. Knezevic, Dual-phase steel sheets under cyclic tension–compression to large strains: experiments and crystal plasticity modeling, J. Mech. Phys. Solid. 96 (2016) 65–87.
[38] A. Eghtesad, M. Knezevic, High-performance full-field crystal plasticity with dislocation-based hardening and slip system back-stress laws: application to modeling deformation of dual-phase steels, J. Mech. Phys. Solid. 134 (2020) 103750.
[39] O. Bouaziz, H. Zurob, M. Huang, Driving force and logic of development of advanced high strength steels for automotive applications, Steel Res. Int. 84 (2013) 937–947.
[40] M. Zecevic, T. Roemer, M. Knezevic, Y. Korkolis, B. Kinsey, Residual ductility and microstructural evolution in continuous-bending-under-tension of AA-6022-T4, Materials 9 (2016) 130.
[41] W.C. Emmens, A.H. van den Boogaard, Incremental forming by continuous bending under tension—an experimental investigation, J. Mater. Process. Technol. 209 (2009) 5456–5463.
[42] J. Benedyk, N. Parikh, D. Stawarz, A method for increasing elongation values for ferrous and nonferrous sheet metals, J. Mater. 6 (1971) 16–29.
[43] H. Swift, Plastic bending under tension, Engineering 166 (1948) 333–359.
[44] H. Nine, Drawbead Forces in Sheet Metal Forming. Mechanics of Sheet Metal Forming, Springer, Boston, MA, 1978, pp. 179–211.
[45] W.C. Emmens, G. Sebastiani, A.H. van den Boogaard, The technology of Incremental Sheet Forming—a brief review of the history, J. Mater. Process. Technol. 210 (2010) 981–997.
[46] J.M. Allwood, D.R. Shouler, A.E. Tekkaya, The increased forming limits of incremental sheet forming processes, Key Eng. Mater. 344 (2007) 621–628.
[47] W.C. Emmens, A.H. van den Boogaard, An overview of stabilizing deformation mechanisms in incremental sheet forming, J. Mater. Process. Technol. 209 (2009) 3688–3695.

[48] T.J. Roemer, T.J. Barrett, M. Knezevic, B.L. Kinsey, Y.P. Korkolis, Experimental study of continuous-bending-under-tension of AA6022-T4, J. Mater. Process. Technol. 266 (2019) 707–714.
[49] M. Knezevic, C.M. Poulin, X. Zheng, S. Zheng, I.J. Beyerlein, Strengthening of alloy AA6022-T4 by continuous bending under tension, Mater. Sci. Eng., A 758 (2019) 47–55.
[50] C.M. Poulin, T.J. Barrett, M. Knezevic, Inferring Post-Necking Strain Hardening Behavior of Sheets by a Combination of Continuous Bending under Tension Testing and Finite Element Modeling, Experimental Mechanics, 2020.
[51] C.M. Poulin, Y.P. Korkolis, B.L. Kinsey, M. Knezevic, Over five-times improved elongation-to-fracture of dual-phase 1180 steel by continuous-bending-under-tension, Mater. Des. 161 (2019) 95–105.
[52] T.J. Barrett, M. Knezevic, Modeling material behavior during continuous bending under tension for inferring the post-necking strain hardening response of ductile sheet metals: application to DP 780 steel, Int. J. Mech. Sci. 174 (2020) 105508.
[53] C.M. Poulin, S.C. Vogel, Y.P. Korkolis, B.L. Kinsey, M. Knezevic, Experimental studies into the role of cyclic bending during stretching of dual-phase steel sheets, Int. J. Material Form. 13 (2020) 393–408.
[54] https://www.ussteel.com/products-solutions/products/dual-phase-1180, 2020.
[55] C. Du, J.P.M. Hoefnagels, S. Kölling, M.G.D. Geers, J. Sietsma, R. Petrov, V. Bliznuk, P.M. Koenraad, D. Schryvers, B. Amin-Ahmadi, Martensite crystallography and chemistry in dual phase and fully martensitic steels, Mater. Char. 139 (2018) 411–420.
[56] L. Morsdorf, E. Emelina, B. Gault, M. Herbig, C.C. Tasan, Carbon redistribution in quenched and tempered lath martensite, Acta Mater. 205 (2021) 116521.
[57] H.-R. Wenk, L. Lutterotti, S. Vogel, Texture analysis with the new HIPPO TOF diffractometer, Nucl. Instrum. Methods Phys. Res. Sect. A Accel. Spectrom. Detect. Assoc. Equip. 515 (2003) 575–588.
[58] N.C. Ferreri, S.C. Vogel, M. Knezevic, Determining volume fractions of γ, γ′, γ″, δ, and MC-carbide phases in Inconel 718 as a function of its processing history using an advanced neutron diffraction procedure, Mater. Sci. Eng., A 781 (2020) 139228.
[59] ASTM E8/E8M-15a, Standard Test Methods for Tension Testing of Metallic Materials, ASTM International, West Conshohocken, PA, 2015.
[60] S. Ghorbanpour, B.A. McWilliams, M. Knezevic, Low-cycle fatigue behavior of rolled WE43-T5 magnesium alloy, Fatig. Fract. Eng. Mater. Struct. 42 (2019) 1357–1372.
[61] T.J. Roemer, Experimental Apparatus for Continuous-Bending-Under-Tension and Experiments on AA6022-T4. Mech. Eng, University of New Hampshire, Durham, NH, 2016. MS.
[62] W.C. Emmens, A.H. van den Boogaard, Cyclic stretch-bending: mechanics, stability and formability, J. Mater. Process. Technol. 211 (2011) 1965–1981.
[63] A. Bhattacharyya, M. Knezevic, M. Abouaf, Characterization of crystallographic texture and intra-grain morphology in cross-rolled tantalum, Metall. Mater. Trans. 46 (2015) 1085–1096.
[64] M. Knezevic, A. Bhattacharyya, Characterization of microstructure in Nb rods processed by rolling: effect of grooved rolling die geometry on texture uniformity, Int. J. Refract. Metals Hard Mater. 66 (2017) 44–51.
[65] M. Knezevic, M. Zecevic, I.J. Beyerlein, A. Bhattacharyya, R.J. McCabe, Predicting texture evolution in Ta and Ta-10W alloys using polycrystal plasticity, JOM 67 (2015) 2670–2674.
[66] M. Knezevic, I.J. Beyerlein, M.L. Lovato, C.N. Tomé, A.W. Richards, R.J. McCabe, A strain-rate and temperature dependent constitutive model for BCC metals incorporating non-Schmid effects: application to tantalum–tungsten alloys, Int. J. Plast. 62 (2014) 93–104.
[67] M. Knezevic, T. Nizolek, M. Ardeljan, I.J. Beyerlein, N.A. Mara, T.M. Pollock, Texture evolution in two-phase Zr/Nb lamellar composites during accumulative roll bonding, Int. J. Plast. 57 (2014) 16–28.
[68] G. Kurdjumow, G. Sachs, Über den mechanismus der stahlhärtung, Z. Phys. 64 (1930) 325–343.
[69] M. Villa, K. Pantleon, M. Reich, O. Kessler, M.A. Somers, Kinetics of anomalous multi-step formation of lath martensite in steel, Acta Mater. 80 (2014) 468–477.
[70] M. Zecevic, M.V. Upadhyay, E. Polatidis, T. Panzner, H. Van Swygenhoven, M. Knezevic, A crystallographic extension to the Olson-Cohen model for predicting strain path dependence of martensitic transformation, Acta Mater. 166 (2019) 386–401.
[71] Z. Feng, M. Zecevic, M. Knezevic, Stress-assisted (γ→α′) and strain-induced (γ→ε→α′) phase transformation kinetics laws implemented in a crystal plasticity model for predicting strain path sensitive deformation of austenitic steels, Int. J. Plast. 136 (2021) 102807.
[72] U. Martin, U. Muhle, H. Oettel, The quantitative measurement of dislocation density in the transmission electron microscope, Prakt. Metallogr. 32 (1995) 467–476.
[73] D. Korzekwa, D. Matlock, G. Krauss, Dislocation substructure as a function of strain in a dual-phase steel, Metall. Mater. Trans. 15 (1984) 1221.
[74] J.W. Christian, S. Mahajan, Deformation twinning, Prog. Mater. Sci. 39 (1995) 1–157.
[75] S. Mahajan, Nucleation and growth of deformation twins in Mo-35 at.% Re alloy, Phil. Mag. 26 (1972) 161–171.